Customized structural reconstruction for IrO_x catalyst using Ni-Co dual coordination towards enhanced water electrolysis in PEM electrolyzers

Yusheng Fang[1], Xiaobing Wu[1], Yingxue Liao[1], Muhammad Imran Abdullah[2], Meiqi Hu[1], Wai Yin Wong[3], Xu Lu[4], Youkun Tao[2*], Jing Shao[1*], Haijiang Wang[5]

[1] College of Chemistry and Environmental Engineering, Shenzhen University, Shenzhen 518060, China

[2] School of Science, Harbin Institute of Technology, Shenzhen 518055, China

[3]Fuel Cell Institute, Universiti Kebangsaan Malaysia, UKM Bangi 43600, Selangor, Malaysia.

[4]Division of Physical Science and Engineering, King Abdullah University of Science and Technology, Thuwal 23955, Saudi Arabia

[5]Department of Mechanical and Energy Engineering, Southern University of Science and Technology, Shenzhen, 518055, China

[*] Corresponding author email: taoyoukun@hit.edu.cn; shaojing@szu.edu.cn

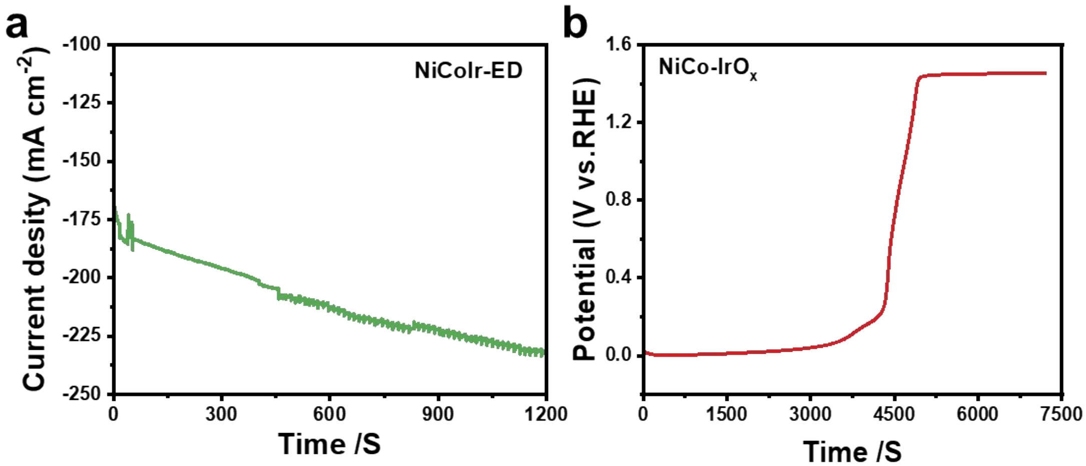

Figure S1. (a) I-t curve during electrodeposition of NiCoIr-ED, (b) Chronopotentiometry curve during electrochemistry dealloying of NiCo-IrO_x.

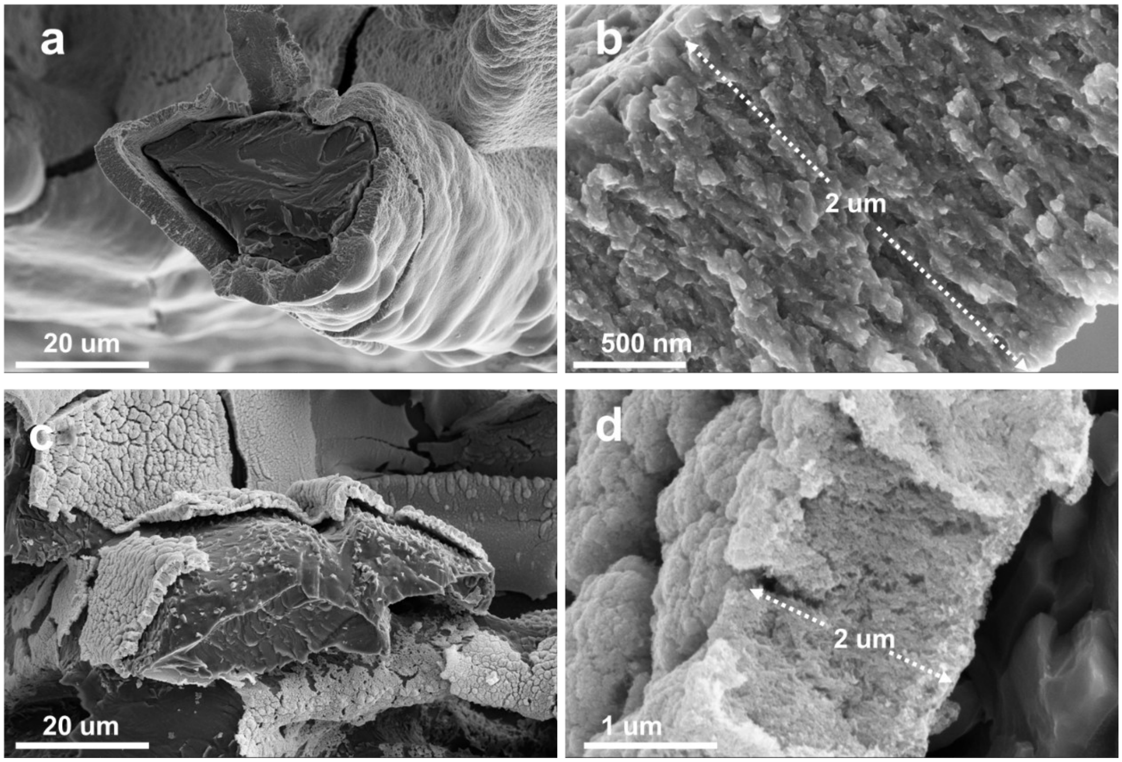

Figure S2. The cross-section SEM images of (a,b) NiCoIr-ED before electrochemical dealloying , (c,d) NiCo-IrO_x after electrochemical dealloying.

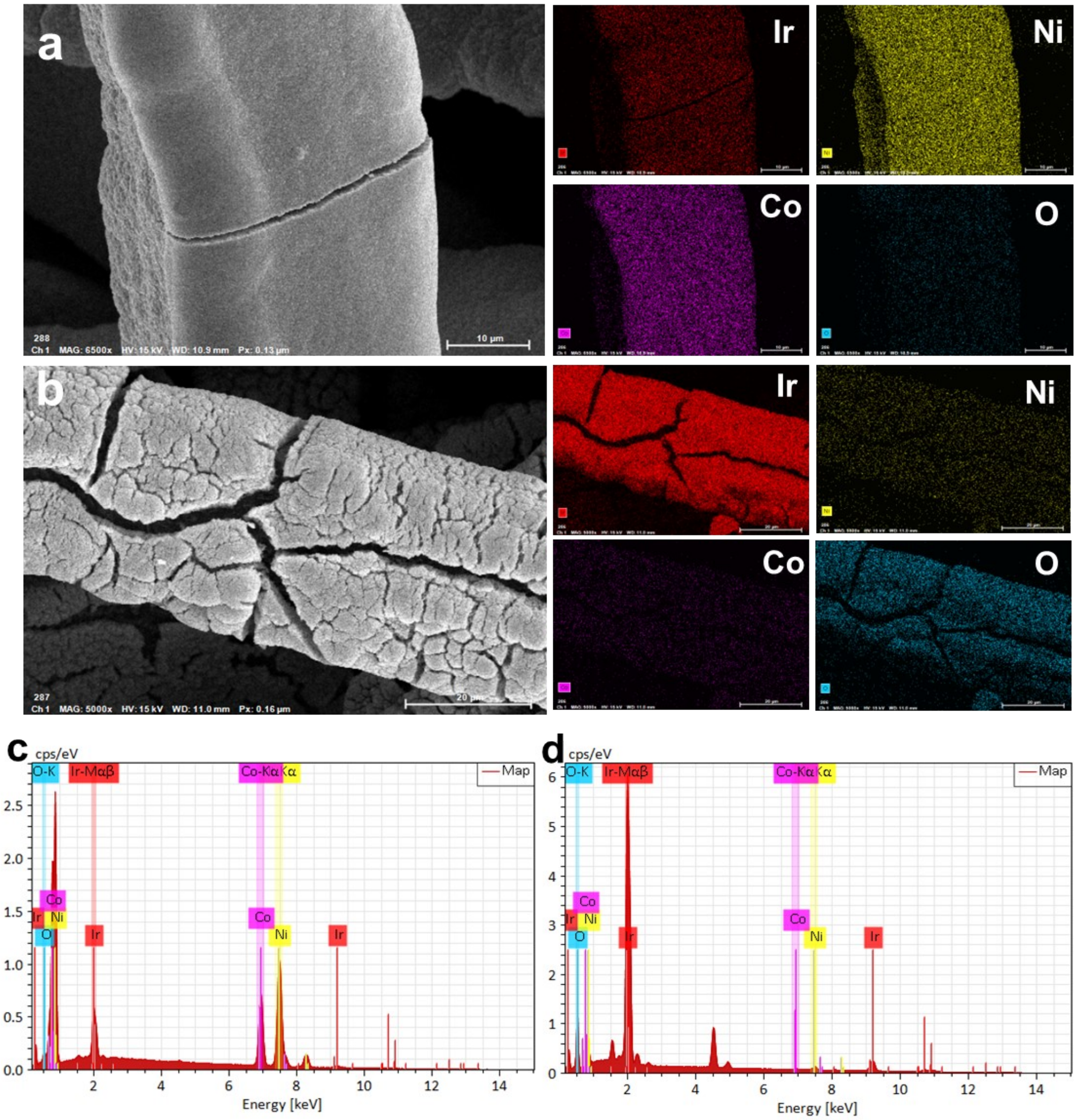

Figure S3. SEM element mapping images of (a,c) NiCoIr-ED before electrochemical dealloying; (b,d) NiCo-IrO_x after electrochemical dealloying.

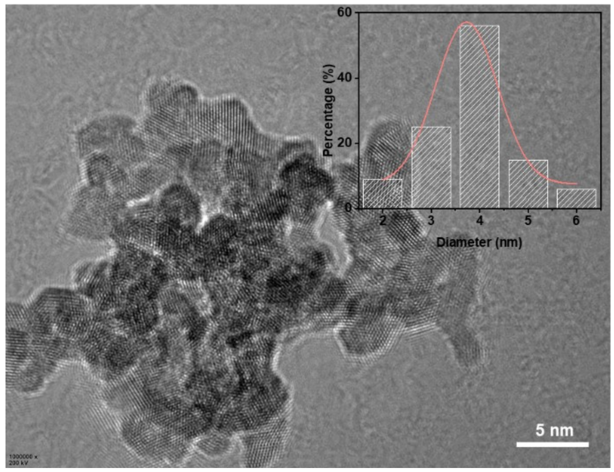

Figure S4. HR-TEM image and Particle size analysis of NiCo-IrO_x.

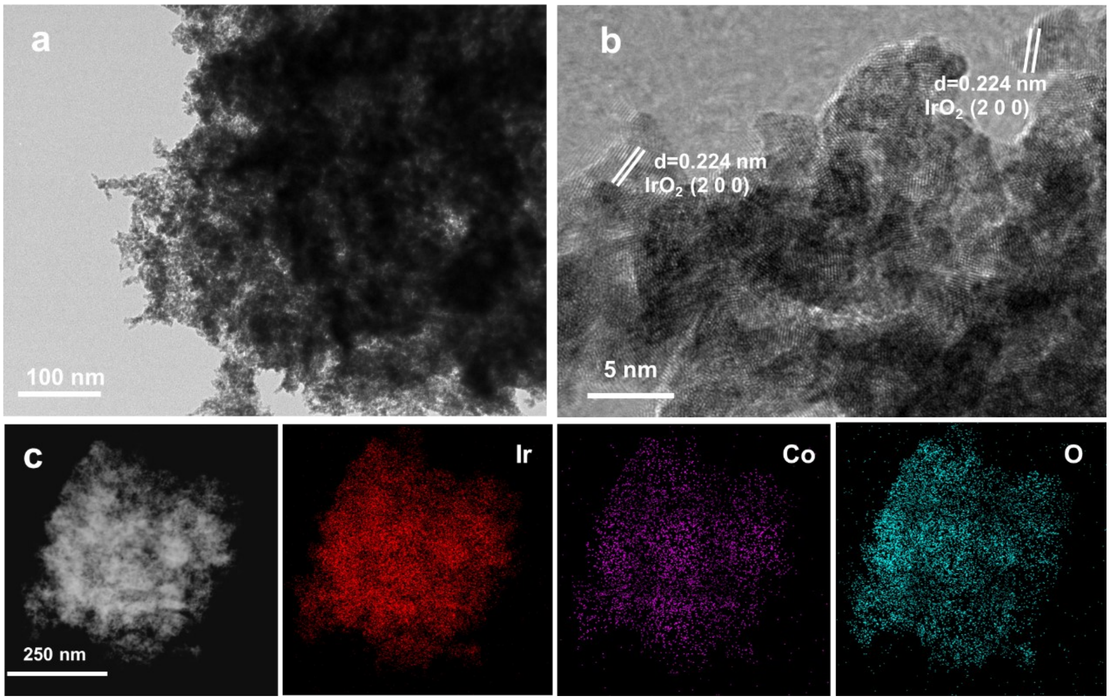

Figure S5. (a, b) TEM images of Co-IrO_x. (c)TEM element mapping images of Co-IrO_x.

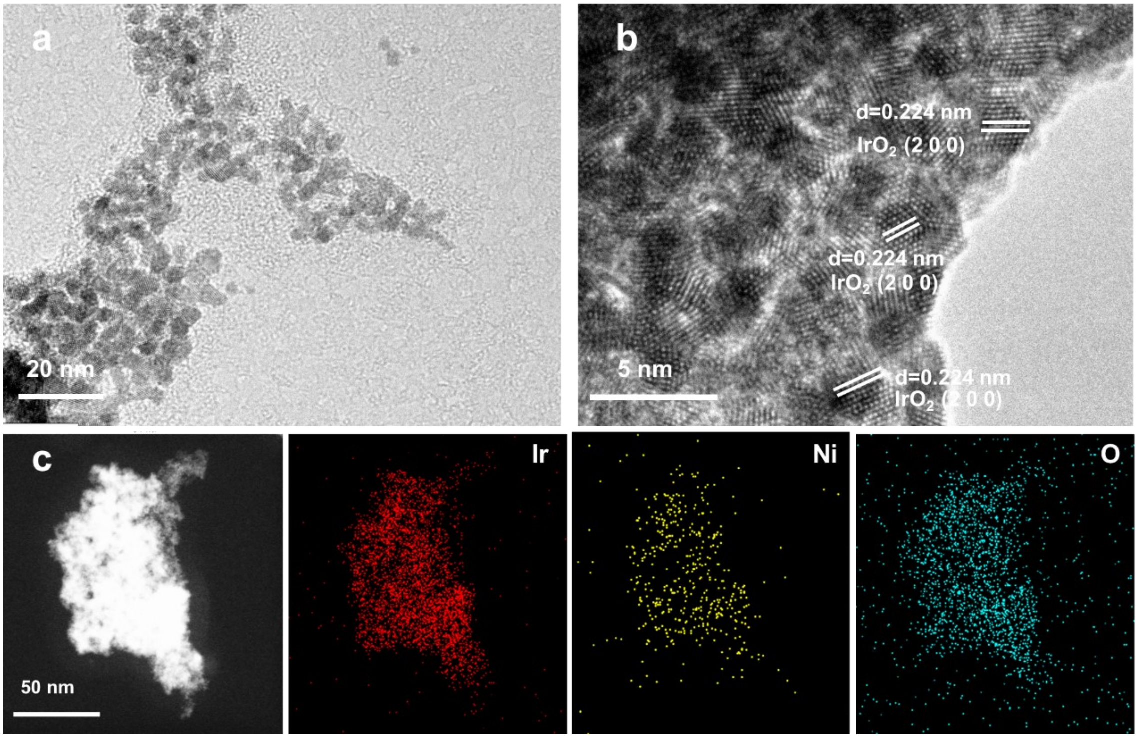

Figure S6. (a, b) TEM images of Ni-IrO_x. (c)TEM element mapping images of Ni-IrO_x.

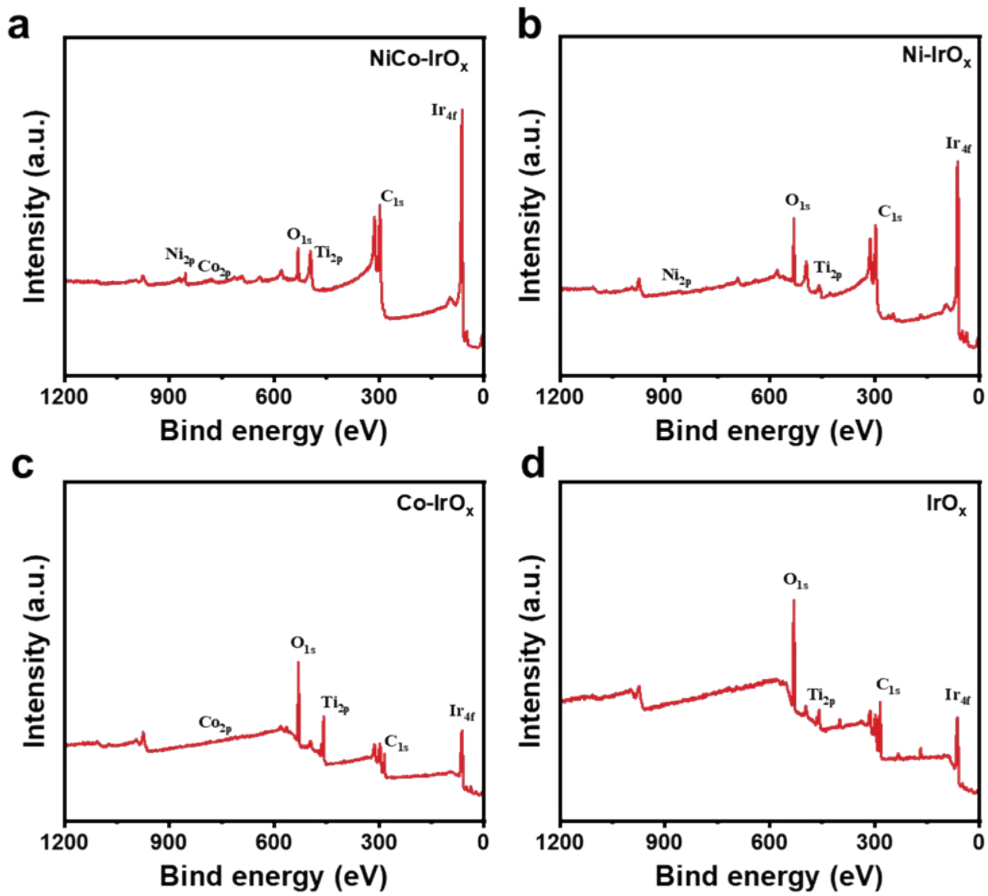

Figure S7. XPS survey spectrum of the (a) NiCo-IrO_x , (b) Ni-IrO_x , (c)Co-IrO_x , (d) IrO_x electrocatalyst.

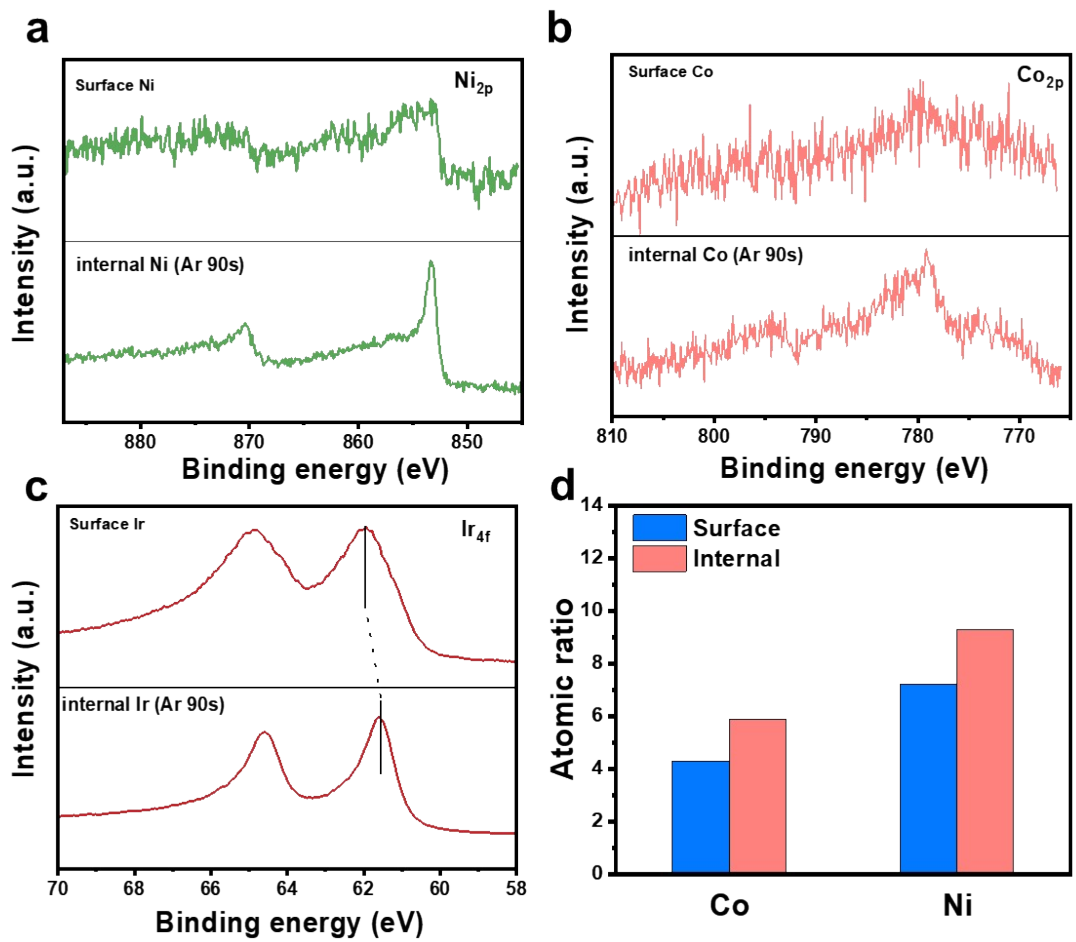

Figure S8. The surface and internal XPS spectra of (a) Ni , (b) Co , (c) Ir for NiCo-IrO_x. (d) The NiCo-IrO_x atomic ratio of Ni and Co in surface and internal.

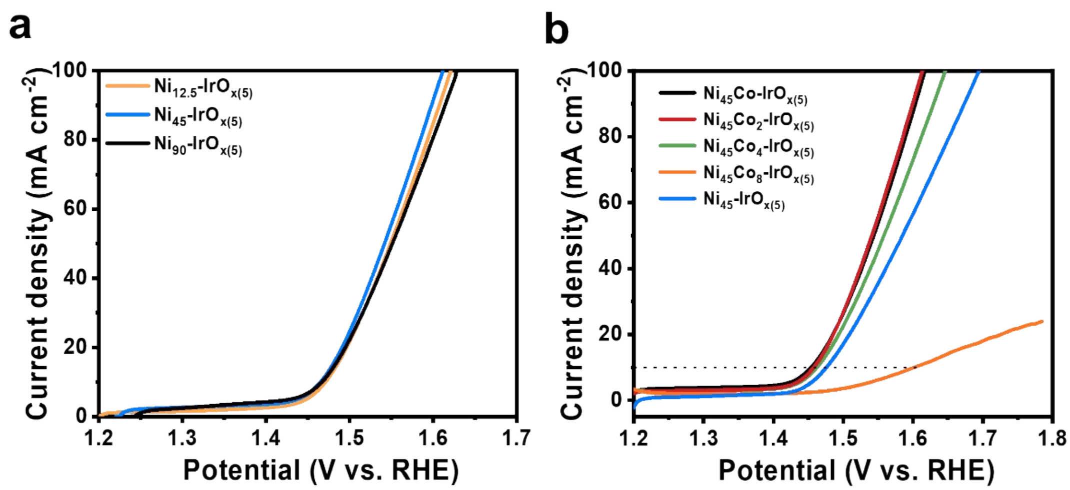

Figure S9. (a) The effect of different Ni content in precursors on electrochemical OER performance of Ni-IrO_x. (b) The effect of different Co content in precursors on electrochemical OER performance of NiCo-IrO_x.

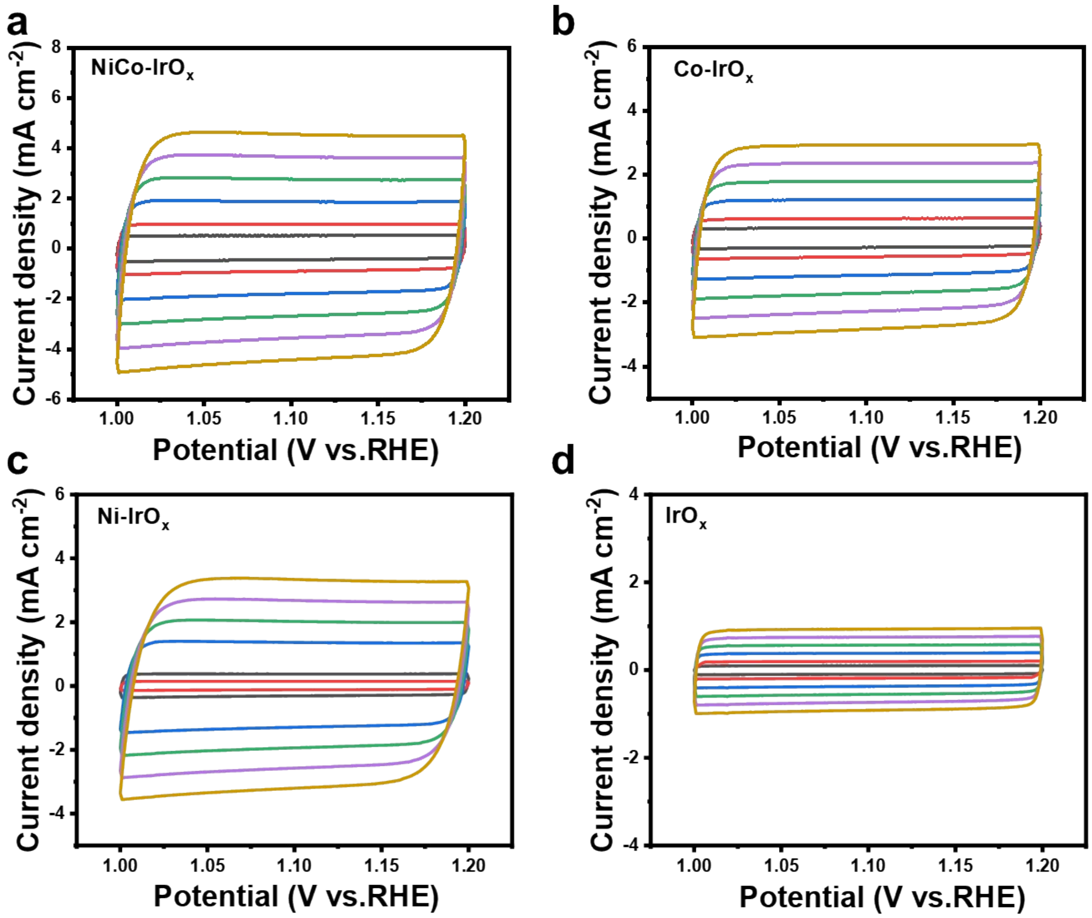

Figure S10. Measurements of electrochemical double layer capacitance of (a)NiCo-IrO_x , (b) Co-IrO_x , (c) Ni-IrO_x and (d) IrO_x.

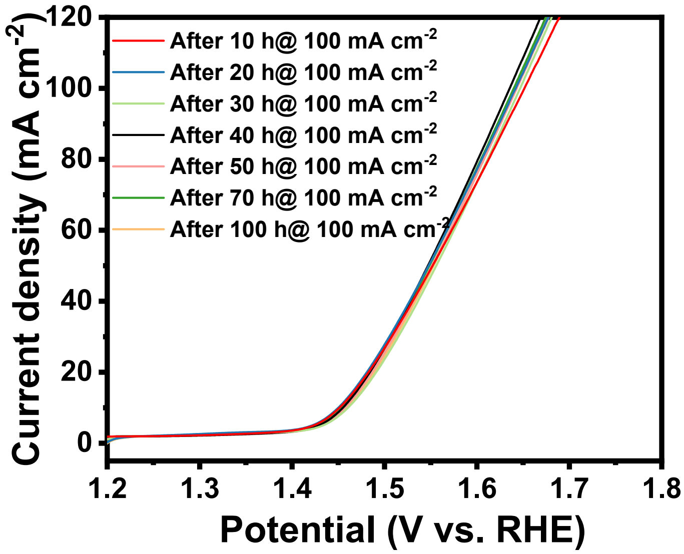

Figure S11. LSV curves of NiCo-IrOx after different stability test durations at a current density of 100 mA cm^{-2}.

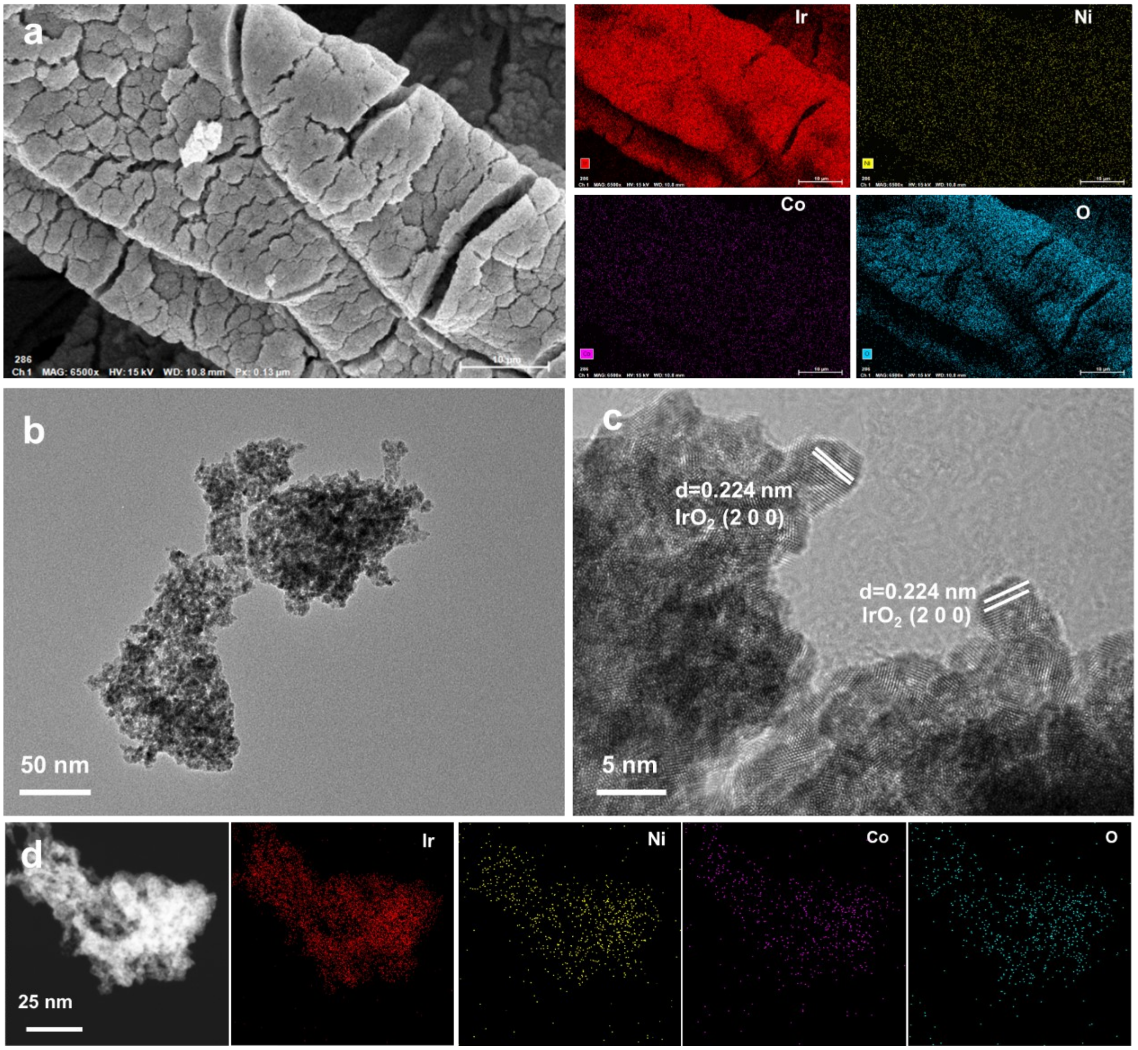

Figure S12. (a) SEM element mapping images of NiCo-IrO_x after 100 h stable test. (b), (c) TEM and HR-TEM images of NiCo-IrO_x after 100 h stable test. (d) TEM element mapping images of NiCo-IrO_x after 100 h stable test.

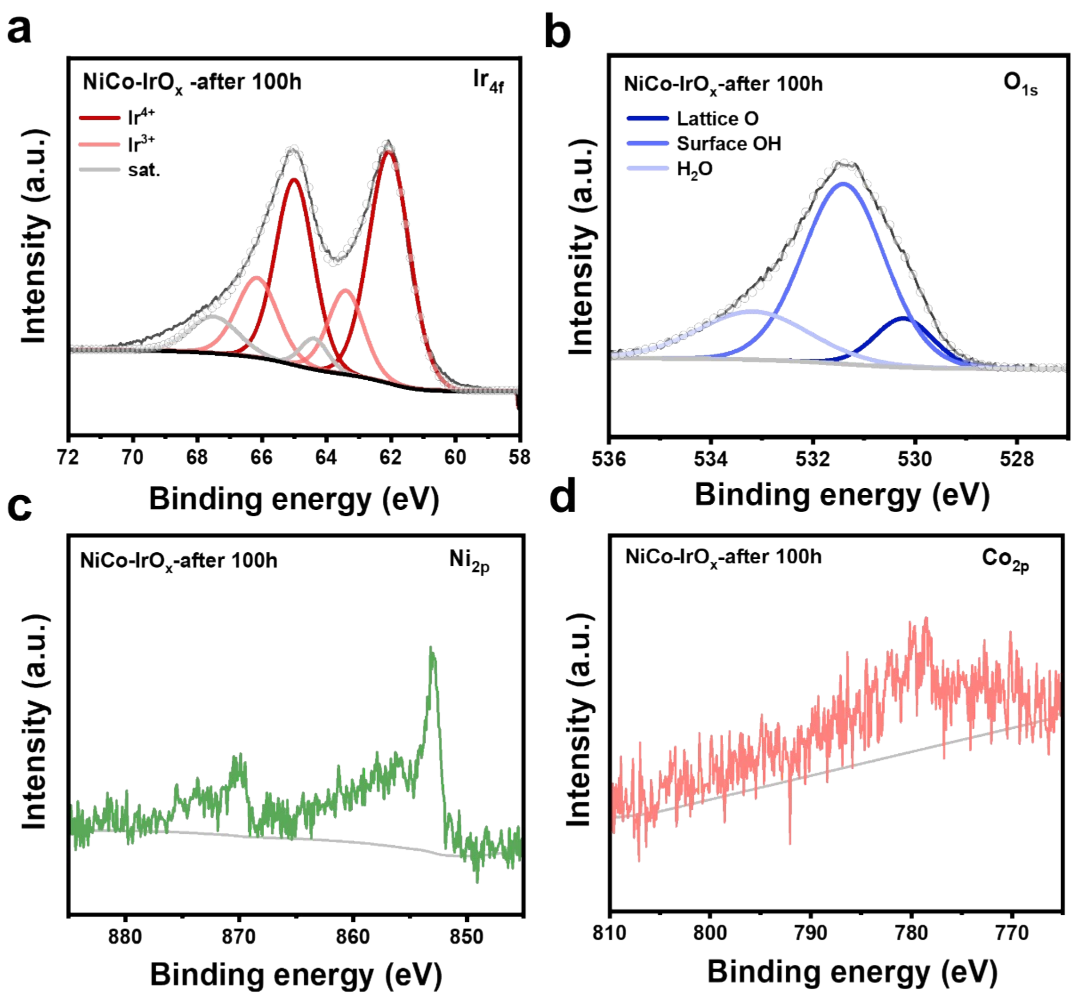

Figure S13. XPS spectra of (a) Ir 4f, (b) O 1s, (c) Ni 2p, (d) Co 2p for NiCo-IrO_x after 100 h.

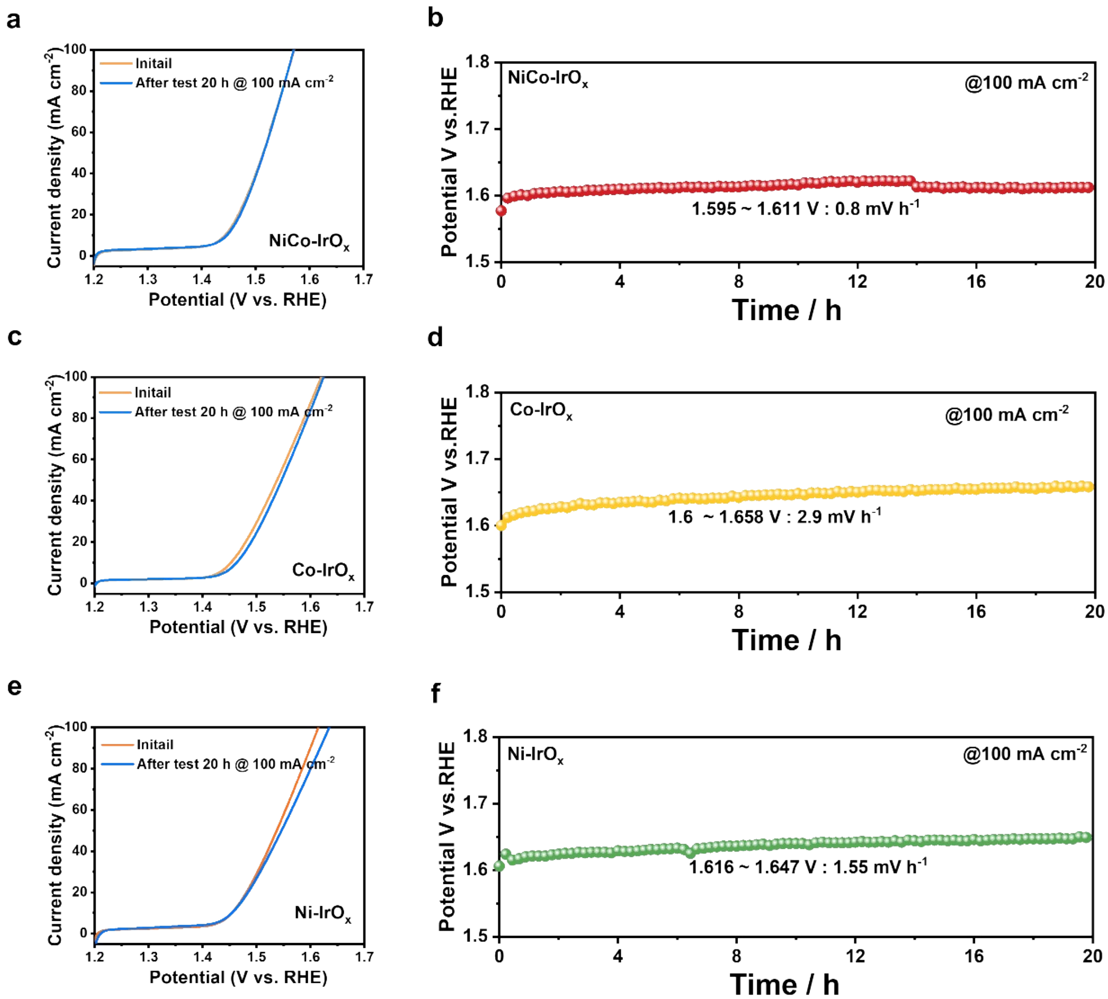

Figure S14. (a) NiCo-IrO_x, (c) Co-IrO_x and (e) Ni-IrO_x LSV test of before and after 100 mA cm^{-2} for 20 h (b) NiCo-IrO_x, (d) Co-IrO_x and (f) Ni-IrO_x: Durability test used a constant current density of 100 mA cm^{-2} for 20 h (without *iR* compensation).

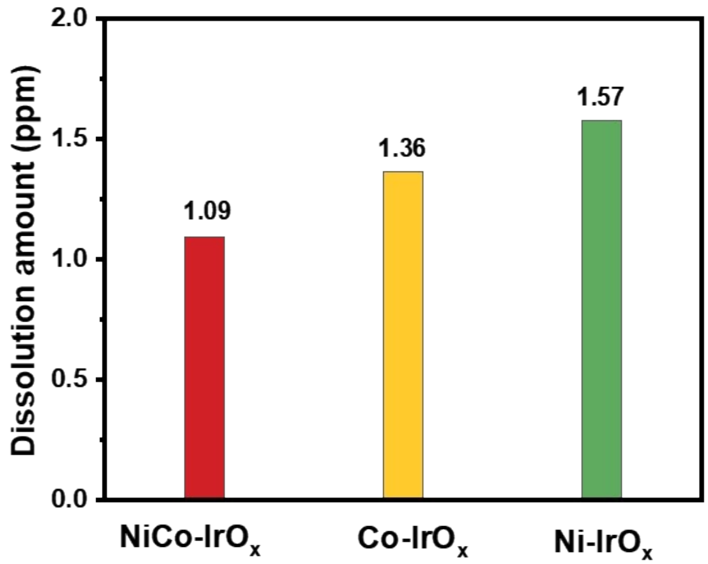

Figure S15. Detected dissolution amount of Ir in the electrolyte after 20 h OER stable test at 100 mA cm^{-2}.

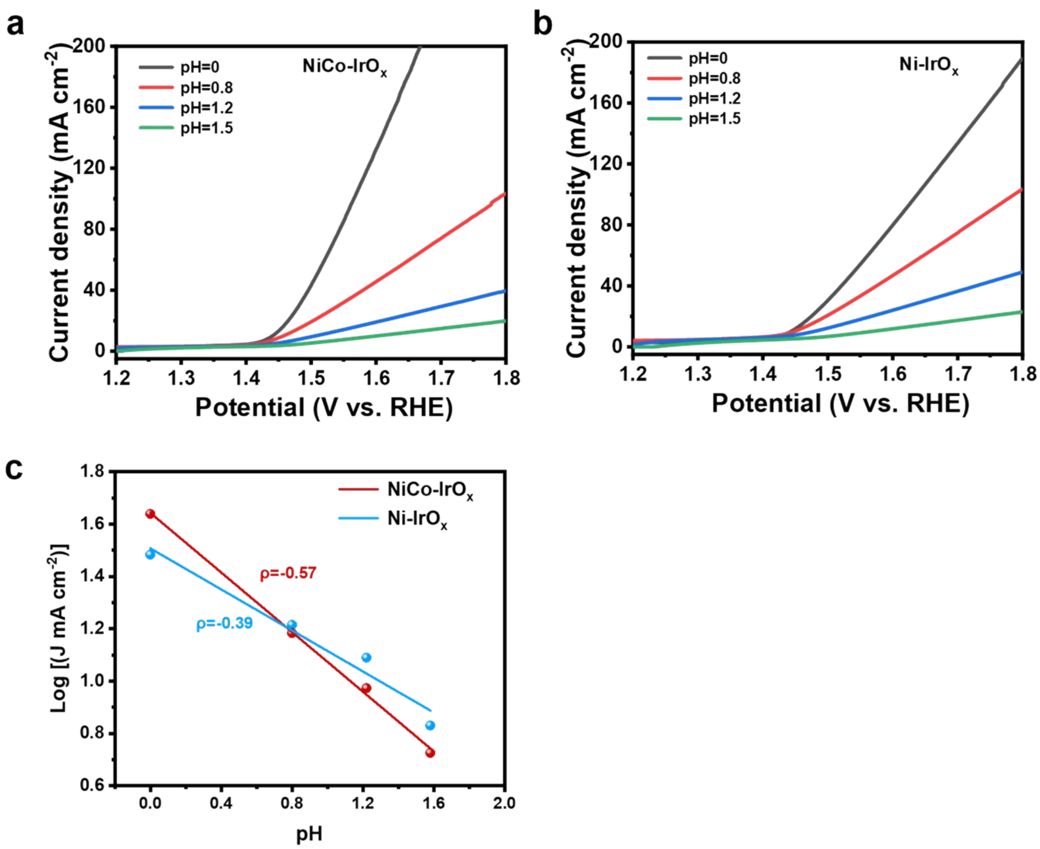

Figure S16. (a-b) The LSV curves of NiCo-IrO$_x$ and Ni-IrO$_x$ at different pH. Scan rate: 5 mV s^{-1}. (c) Logarithm of current density as a function of pH.

.

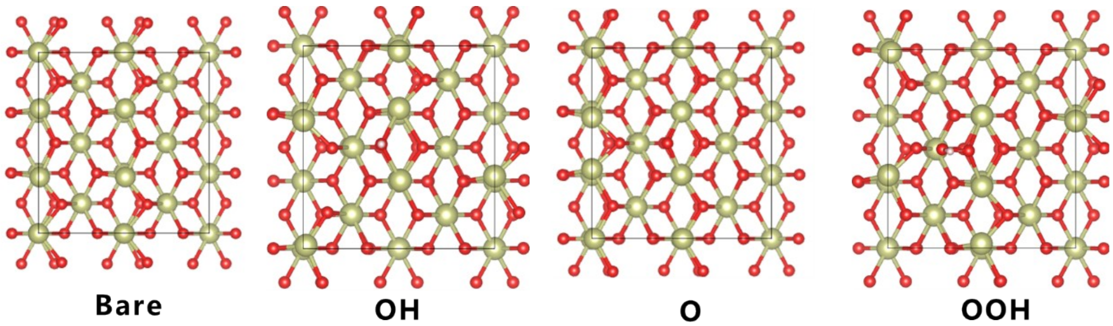

Figure S17. Top view of the bare and adsorption states of *OH, *O, and *OOH of the OER process of IrO_2.

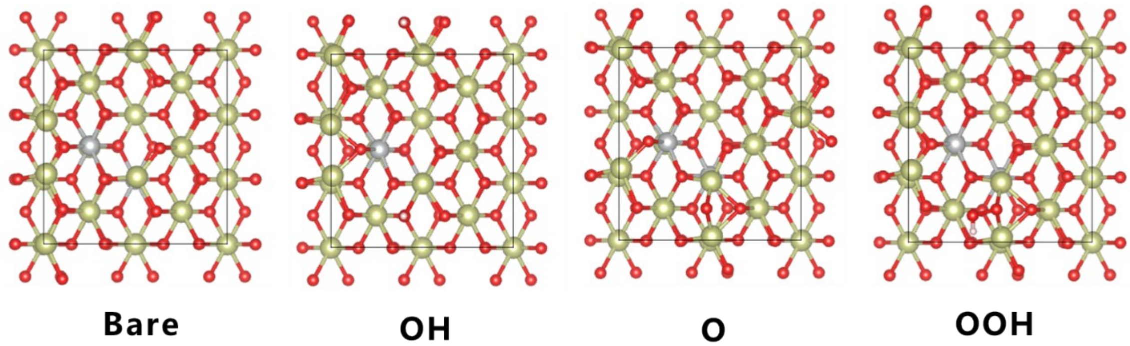

Figure S18. Top view of the bare and adsorption states of *OH, *O, and *OOH of the OER process of Ni-IrO_x.

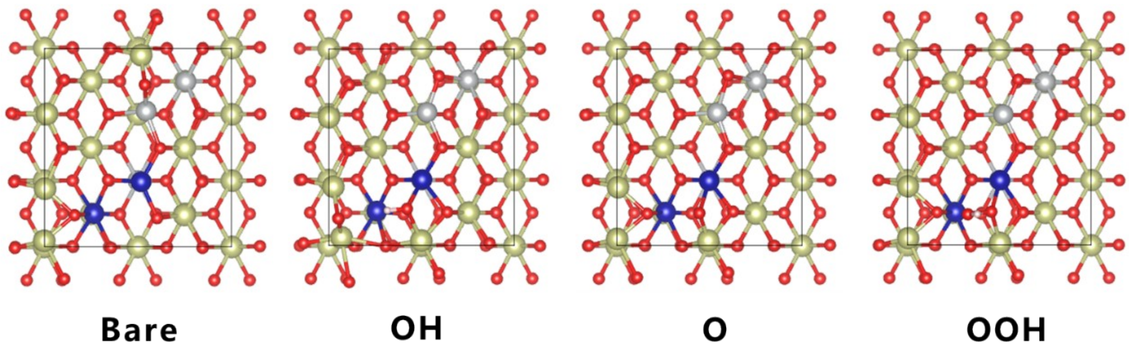

Figure S19. Top view of the bare and adsorption states of *OH, *O, and *OOH of the OER process of NiCo-IrO_x.

Table S1 . The atomic ratio of NiCoIr-ED obtained from the TEM-EDX analysis in Figure 2e.

atom ratio	NiCoIr-ED		
	Ir	Co	Ni
EDX	5%	17.8%	77.2%

Table S2 . NiCo-IrOx atomic ratio from ICP and TEM-EDX analysis

atom ratio	NiCo-IrO_x		
	Ir	Co	Ni
ICP	89%	3.4%	7.6%
EDX	90.4%	3.6%	6%

Table S3. Summaries of XPS fitting results on NiCo-IrO_x, Co-IrO_x, Ni-IrO_x, IrO_x samples

Sample	NiCo-IrO_x	Co-IrO_x	Ni-IrO_x	IrO_x
$Ir^{4+}/Ir^{3+}+Ir^{4+}$	0.869	0.862	0.617	0.565
$O_{OH}/O_{Lat}+O_{OH}+O_{H_20}$	0.480	0.399	0.301	0.232

Table S4. Parameters used to fit the XPS spectra (Ir4f band). The specific fit parameters used for IrO_2. The doublet separation between $Ir4f_{7/2}$ and $Ir4f_{5/2}$ was considered to be 3.0 eV and the height ratio between $Ir4f_{7/2}$ and $Ir4f_{5/2}$ peaks was 0.75.

Peak	Binding Energy (EV)				FWHM (EV)				Face Ratio			
	NiCo-IrOx	Co-IrOx	Ni-IrOx	IrOx	NiCo-IrOx	Co-IrOx	Ni-IrOx	IrOx	NiCo-IrOx	Co-IrOx	Ni-IrOx	IrOx
Ir $4f_{7/2}$ Ir (Ⅳ)	61.9	61.8	61.6	61.6	1.27	1.21	1.2	1.1	1	1	1	1
Ir $4f_{5/2}$ Ir (Ⅳ)	65.9	64.8	64.6	64.6	1.27	1.21	1.2	1.1	0.75	0.75	0.75	0.75
Ir $4f_{7/2}$ Ir (Ⅲ)	62.6	62.5	62.6	62.4	1.17	1.14	1.18	1.08	0.39	0.45	0.83	0.82
Ir $4f_{5/2}$ Ir (Ⅲ)	65.6	65.5	65.6	65.4	1.17	1.14	1.18	1.08	0.29	0.33	0.62	0.61
Ir $4f_{7/2}$ Ir (Ⅲ+Ⅳ)sat	63.9	63.8	63.6	63.6	1.6	1.5	1.58	1.52	0.44	0.51	0.52	0.42
Ir $4f_{5/2}$ Ir (Ⅲ+Ⅳ)sat	66.9	66.8	63.6	66.6	1.6	1.5	1.58	1.52	0.44	0.48	0.52	0.42

Table S5. Comparison of OER activity and stability of NiCo-IrO_x with literature-reported Ir-based electrocatalysts and the corresponding conditions in acidic electrolytes.

Catalyst	η_{10} mV	Substr-ate	Tafel slope	Mass activity (A g^{-1}) (η = 270 mV)	Electrolyte	Stability	Ref
NiCo-IrO_x	209	Ti- felt	53	258.42	0.5 M H_2SO_4	100 h@ 100 mA cm^{-2}	This work
Dotf-$IrCo_5$	250	-	-	165.13	0.5 M H_2SO_4	30 h@10 mA cm^{-2}	Ref[1]
Ir-Fe aerogels	236	GC	76.8	0.59	0.5 M H_2SO_4	100 h@10 mA cm^{-2}	Ref[2]
ZnNiCoIr Mn	237	GC	46	610.8	0.1 M $HClO_4$	100 h@10 mA cm^{-2}	Ref[3]
Ti-IrOx/Ir	254	GC	48	338 (η=350 mV)	0.5 M H_2SO_4	24 h@10 mA cm^{-2}	Ref[4]
IrCo@ CNT/CC	241	CC	92	~1	0.5 M H_2SO_4	90 h@10 mA cm^{-2}	Ref[5]
DNP-IrNi	248	Ti-felt	38	52.48	0.5 M H_2SO_4	50 h@100 mA cm^{-2}	Ref[6]
NiIr-ENS	224	GC	91.2	4.62 (η= 320 mV)	0.5 M H_2SO_4	3000 cycle	Ref[7]
IrCo NRAs	296	CC	68.1	0.84	0.5 M H_2SO_4	15 h@10 mA cm^{-2}	Ref[8]
Ir−Ni−Co oxide	285	GC	53	~55	0.1 M $HClO_4$	5.5 h@10 mA cm^{-2}	Ref[9]
Ir@WO_x NRs-100	330	WO_x	46.8	-	0.5 M H_2SO_4	40 h	Ref[10]

Co-IrRu	235	GC	66.9	-	0.1 M $HClO_4$	25 h@10 mA cm^{-2}	Ref[11]
IrNi NFs	293	GC	47.3	379 (η=280 mV)	0.1 M $HClO_4$	4 h@20 mA cm^{-2}	Ref[12]

Table S6. Comparison of HER activity and stability of NiCo-IrO_x with literature-reported Ir-based electrocatalysts and the corresponding conditions in acidic electrolytes.

Catalyst	**η_{10} mV**	**Substr-ate**	**Tafel slope**	**Mass activity (A g^{-1}) (η = 50 mV)**	**Electrolyte**	**Stability**	**Ref**
NiCo-IrO_x	37	Ti- felt	26.3	37.37	0.5 M H_2SO_4	20 h@100 mA cm^{-2}	This work
ZnNiCoIrMn	50@50 mV	GC	30.6	-	0.1 M $HClO_4$	100 h@10 mA cm^{-2}	Ref[3]
IrCo@CNT/CC	26	GC	45.2	~ 1.2	0.5 M H_2SO_4	90 h@10 mA cm^{-2}	Ref[5]
DNP-IrNi	15	Ti-felt	28.4	-	0.5 M H_2SO_4	-	Ref[6]
NiIr-ENS	10	GC	28.2	-	0.5 M H_2SO_4	3000 cycle	Ref[7]
Co-IrRu	13.8	GC	31.1	- -	0.1 M $HClO_4$	25 h@10 mA cm^{-2}	Ref[11]

IrNi NFs	25	GC	29.7	-		0.1 M $HClO_4$	6 h@10 mA cm^{-2}	Ref[12]
$IrCo_{0.65}$	17	GC	31.2	-		0.1 M $HClO_4$	20000 s @10 mA cm^{-2}	Ref[13]

reference

(1) Kim, K.-S.; Park, S.-A.; Jung, H. D.; Jung, S.-M.; Woo, H.; Ahn, D.; Park, S. S.; Back, S.; Kim, Y.-T. Promoting oxygen evolution reaction induced by synergetic geometric and electronic effects of IrCo thin-film electrocatalysts. *ACS Catal.* **2022**, *12* (11), 6334-6344.

(2) Gao, C. Y.; Wang, J.; Hübner, R.; Zhan, J. H.; Zhao, M. W.; Li, Y. Y.; Cai, B. Spin Effect to Regulate the Electronic Structure of Ir—Fe Aerogels for Efficient Acidic Water Oxidation. *Small* **2024**, *20* (33), 2400875.

(3) Kwon, J.; Sun, S.; Choi, S.; Lee, K.; Jo, S.; Park, K.; Kim, Y. K.; Park, H. B.; Park, H. Y.; Jang, J. H.; et al. Tailored electronic structure of Ir in high entropy alloy for highly active and durable bifunctional electrocatalyst for water splitting under an acidic environment. *Adv. Mater* **2023**, *35* (26), 2300091.

(4) Wang, Y. B.; Ma, R. P.; Shi, Z. P.; Wu, H. X.; Hou, S.; Wang, Y.; Liu, C. P.; Ge, J. J.; Xing, W. Inverse doping IrO_x/Ti with weakened Ir-O interaction toward stable and efficient acidic oxygen evolution. *Chem* **2023**, *9* (10), 2931-2942.

(5) Wang, X.; Qin, Z.; Qian, J. J.; Chen, L. Y.; Shen, K. IrCo nanoparticles encapsulated with carbon nanotubes for efficient and stable acidic water splitting. *ACS Catal.* **2023**, *13* (16), 10672-10682.

(6) Yeo, K.-R.; Lee, K.-S.; Kim, H.; Lee, J.; Kim, S.-K. A highly active and stable 3D dandelion spore-structured self-supporting Ir-based electrocatalyst for proton exchange membrane water electrolysis fabricated using structural reconstruction. *Energy Environ. Sci* **2022**, *15* (8), 3449-3461.

(7) Xie, Y. H.; Feng, Y. M.; Jin, S. Y.; Li, C.; Li, C. S.; Sun, Y.; Luo, F.; Yang, Z. H. Nickel-doped iridium echinus-like nanosheets for stable acidic water splitting. *Chemical Communications* **2023**, *59* (54), 8404-8407.

(8) Zhang, Y.; Zhang, G.; Zhang, M.; Zhu, X.; Shi, P.; Wang, S.; Wang, A.-L. Synergistic electronic and morphological modulation by trace Ir introduction boosting oxygen evolution performance over a wide pH range. *Chemical Engineering Journal* **2022**, *433*, 133577.

(9) Zaman, W. Q.; Wang, Z. Q.; Sun, W.; Zhou, Z. H.; Tariq, M.; Cao, L. M.; Gong, X. Q.; Yang, J. Ni-Co codoping breaks the limitation of single-metal-doped IrO_2 with higher oxygen evolution reaction performance and less iridium. *ACS Energy Lett.* **2017**, *2* (12), 2786-2793.

(10) Jiang, G.; Yu, H. M.; Li, Y. H.; Yao, D. W.; Chi, J.; Sun, S. C.; Shao, Z. G. Low-Loading and highly stable membrane electrode based on an Ir@WO_x NR ordered array for PEM water electrolysis. *ACS Appl. Mater. Interfaces* **2021**, *13* (13), 15073-15082.

(11) Shan, J. Q.; Ling, T.; Davey, K.; Zheng, Y.; Qiao, S. Z. Transition-metal-doped RuIr bifunctional nanocrystals for overall water splitting in acidic environments. *Adv. Mater* **2019**, *31* (17), 1900510.

(12) Lv, F.; Zhang, W.; Yang, W.; Feng, J.; Wang, K.; Zhou, J.; Zhou, P.; Guo, S. Ir-Based Alloy Nanoflowers with Optimized Hydrogen Binding Energy as Bifunctional Electrocatalysts for Overall Water Splitting. *Small Methods* **2020**, *4* (6), 1900129.

(13) Fu, L. H.; Zeng, X.; Cheng, G. Z.; Luo, W. IrCo Nanodendrite as an Efficient Bifunctional Electrocatalyst for Overall Water Splitting under Acidic Conditions. *ACS Appl. Mater. Interfaces* **2018**, *10* (30), 24993-24998.